Eur. Phys. J. B (2019) 92: 142
https://doi.org/10.1140/epjb/e2019-100123-7

THE EUROPEAN PHYSICAL JOURNAL B

Regular Article

Shrinkage mechanisms of grain boundary loops in two-dimensional colloidal crystals*

François A. Lavergne, Arran Curran, Dirk G.A.L. Aarts, and Roel P.A. Dullens[a]

Department of Chemistry, Physical and Theoretical Chemistry Laboratory, University of Oxford, South Parks Road, Oxford OX1 3QZ, UK

Received 28 February 2019 / Received in final form 8 May 2019
Published online 1 July 2019

Abstract. We discuss the various mechanisms involved in the spontaneous shrinkage of circular grain boundaries in two-dimensional colloidal crystals. We provide experimental evidence that these grain boundary loops shrink owing to three intermittent mechanisms proposed for atomic materials, namely purely curvature-driven migration, coupled grain boundary migration, and grain boundary sliding. Throughout shrinkage, the product of the radius and misorientation of the grain boundary loop remains higher than a fundamental limit resulting from the specific dislocation structure of grain boundary loops, except for the very last stage where the loop character is lost. Despite its complexity, this process can be effectively described by a single kinetic coefficient, allowing for a simplified description of grain boundary loop kinetics.

1 Introduction

It is well accepted that grain growth is driven by the migration and annihilation of grain boundaries (GBs) [1]. In absence of an external driving force, the migration of GBs is generally attributed to capillary forces induced by their own curvature [2,3]. However, due to the mismatch of the two adjacent crystals, GBs possess a dislocation structure that is affected during their migration and annihilation, via dislocation reactions [4–6]. This additional complexity may lead to other modes of GB motion, such as grain rotation or coupling between migration and rotation [7], the relative contributions of which remain unclear.

In this respect, circular GBs in two-dimensional materials have attracted a lot of interest since their fixed curvature provides a natural driving force for their migration. In the sole presence of capillary forces, the area enclosed by such a "GB loop" [8] is expected to decrease at a constant rate, the reduced mobility M^* [9–11]. The latter depends on the misorientation between the inner and outer crystals in a way that is still unclear since both an increase [5] and a decrease [12] have been reported in simulations. GB loops are also convenient to study the reactions between dislocations, since the latter are forced to annihilate until a single crystal is left, which has been investigated fairly recently using simulations [5,13]. Experimentally, the creation and shrinkage of GB loops have been achieved in graphene under electron irradiation at high temperatures [14,15]. However, the time resolution of the shrinkage process remains low and these methods do not allow for the control of the misorientation.

A promising route to prepare such GB loops is to use model systems such as colloidal crystals, which can readily be manipulated using external fields, owing to their inherent softness [16]. Various optical tweezing methods have been used to induce local melting [17], or create dislocations and GBs in a colloidal crystal [18]. It is also possible to create GB loops using holographic optical tweezers [18] or "optical blasting" [19], though controlling their size and misorientation remains challenging. The latter is nevertheless necessary to explore the initial conditions leading to potentially different modes of GB migration and shrinkage, which can be directly monitored using simple video-microscopy. An additional advantage compared to atomic materials is that shrinkage happens spontaneously at room temperature in these soft colloidal crystals.

In this article, we study the different shrinkage mechanisms of GB loops with well-defined sizes and misorientations, created in two-dimensional colloidal crystals using optical vortices. The spontaneous shrinkage of these GB loops is subsequently monitored with single particle resolution using video-microscopy. We find that the shrinkage can be characterised by a reduced mobility as a single kinetic coefficient, despite being the result of many different processes. In particular, we show the presence of curvature-driven migration, coupled GB migration, and grain rotation by GB sliding in this colloidal crystal with simple hard sphere interactions. Importantly, the product of the misorientation and the size of the grain boundary

* Contribution to the Topical Issue "Multiscale Materials Modeling", edited by Yoji Shibutani, Shigenobu Ogata, and Tomotsugu Shimokawa.

[a] e-mail: roel.dullens@chem.ox.ac.uk

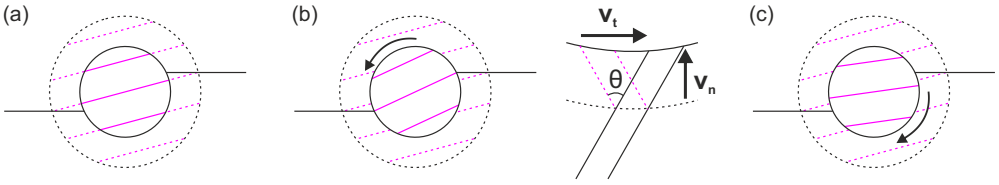

Fig. 1. (a) Circular grain before (dashed circle) and after (solid circle) pure curvature-driven shrinkage (no grain rotation). The black solid lines represent rows of the outer crystal after shrinkage. The magenta lines illustrate the orientation of the circular grain before (dashed lines) and after shrinkage (solid lines). The continuity of crystal rows is broken during the process. (b) Illustration of coupled GB migration, where the continuity of crystal rows is ensured by grain rotation towards higher angles (black arrow). The tangential velocity v_t and the normal velocity v_n are related by $v_t = 2\tan(\theta/2)v_n$, where θ is the misorientation. (c) Illustration of GB sliding where shrinkage is accompanied by grain rotation towards lower angles (black arrow), breaking the continuity of crystal rows.

loop is always larger than or equal to $3\sigma/\pi$, where σ is the lattice spacing, except at the final stage where the loop character is lost. This value is a geometric limit on the formation and existence of grain boundary loops in two-dimensional hexagonal crystals [20].

2 Mechanisms of grain boundary loop shrinkage

We start by revisiting the three main mechanisms that may come into play during the shrinkage of a GB loop, namely pure curvature-driven shrinkage, coupled GB migration, and GB sliding [5,7]. For the sake of clarity, they are treated independently here, despite the fact that they can contribute simultaneously or intermittently.

2.1 Curvature-driven shrinkage

In the case of pure curvature-driven shrinkage, i.e. without grain rotation, the normal velocity of the GB v_n is proportional to its curvature κ according to

$$v_n = M_n \Gamma \kappa, \tag{1}$$

where M_n is the mobility corresponding to normal motion and Γ is the GB stiffness [7,21]. The driving force for GB migration is then the capillary pressure given by $\Gamma\kappa$ and M_n can be seen as an inverse friction coefficient per unit length of GB. For a circular GB loop of radius R, $v_n = -\mathrm{d}R/\mathrm{d}t$ and $\kappa = 1/R$ so that

$$\frac{\mathrm{d}R}{\mathrm{d}t} = -\frac{M_n\Gamma}{R}. \tag{2}$$

Note that Γ in equation (2) denotes the stiffness averaged along the loop, which for a perfectly circular GB loop reduces to the interfacial free energy. Assuming that the product $M_n\Gamma$ is constant during shrinkage, integration of equation (2) gives the law of parabolic shrinkage

$$R^2(t) = R^2(0) - 2M^*t, \tag{3}$$

where $M^* = M_n\Gamma$ is the reduced mobility [11]. As a consequence, the area enclosed by the GB loop $A = \pi R^2$ decreases at constant rate given by [9]

$$\frac{\mathrm{d}A}{\mathrm{d}t} = -2\pi M^*. \tag{4}$$

The reduced mobility M^* can thus be seen as a rate of shrinkage per unit of solid angle along the GB contour. The illustration of pure curvature-driven grain shrinkage in Figure 1a shows that the GB motion in absence of grain rotation leads to a discontinuity of crystal rows during shrinkage.

2.2 Coupled grain boundary migration

Coupled GB migration is a migration mode for which the continuity of the crystal rows is maintained between the central grain and the outer crystal. This purely geometrical constraint implies that the tangential velocity and the normal velocity of the GB are proportional

$$v_t = \beta v_n, \tag{5}$$

where β is the coupling factor [7]. As illustrated in Figure 1b, the requirement for the continuity of crystal rows yields

$$\tan\left(\frac{\theta}{2}\right) = \frac{v_t}{2v_n}, \tag{6}$$

which gives the expression for the coupling factor: $\beta = 2\tan(\theta/2)$ [7]. As for a circular grain $v_n = -\mathrm{d}R/\mathrm{d}t$ and $v_t = R\mathrm{d}\theta/\mathrm{d}t$, equation (5) can be rewritten as

$$R\frac{\mathrm{d}\theta}{\mathrm{d}t} = -2\tan\left(\frac{\theta}{2}\right)\frac{\mathrm{d}R}{\mathrm{d}t}. \tag{7}$$

Integration of equation (7) results in

$$R(t)\sin\left(\frac{\theta(t)}{2}\right) = R(0)\sin\left(\frac{\theta(0)}{2}\right), \tag{8}$$

where $t = 0$ corresponds to the beginning of coupled migration. Equation (8) means that the quantity $R\sin(\theta/2)$ is conserved during coupled migration. Hence, as R decreases, the grain *always* rotates towards *higher* misorientations (see Fig. 1b). It has been reported that

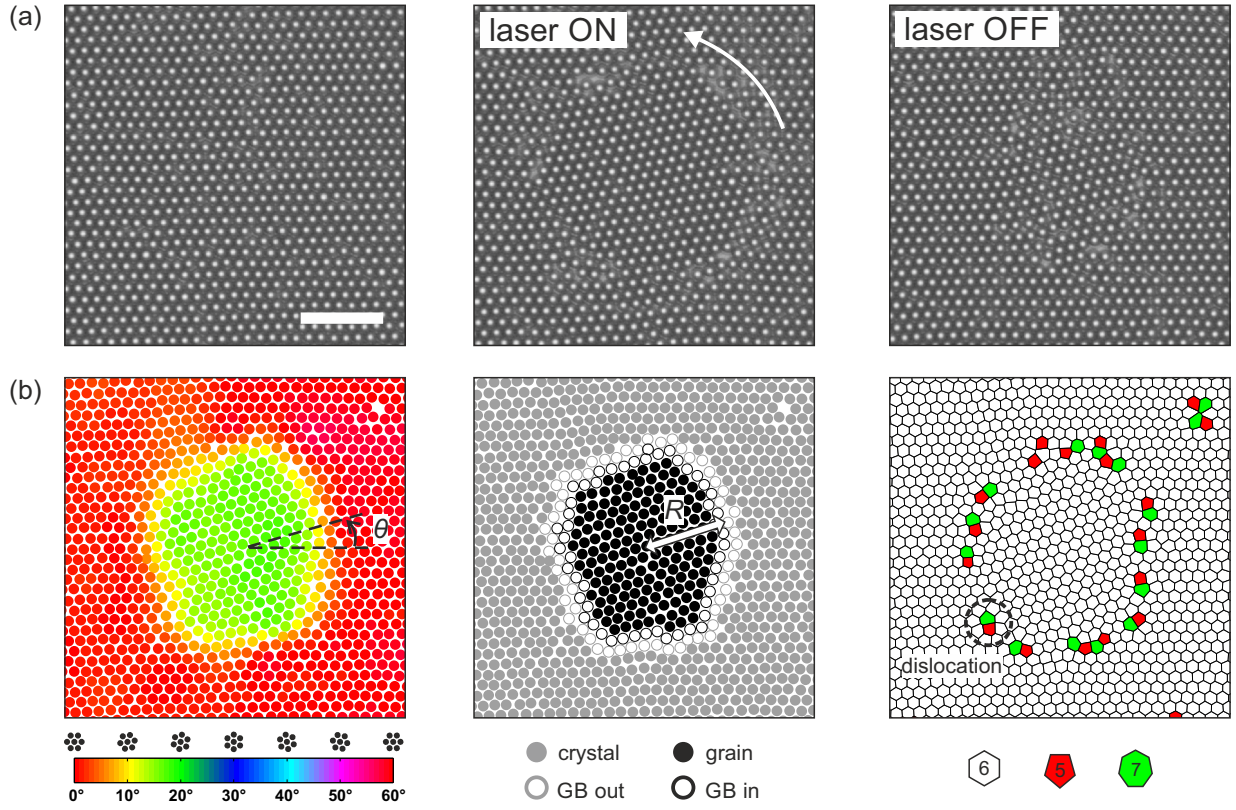

Fig. 2. (a) Starting from a colloidal crystal (left), a GB loop is formed by rotating a circular portion of crystal using an optical vortex (centre). After the laser beam is turned off, the GB loop spontaneously shrinks (right). Scale bar, 20 μm. (b) Image analysis to extract the characteristics of the GB loop. Misorientation θ as obtained from the local crystalline orientation θ_6 indicated by the colourbar (left), detection of the GB loop and radius R (centre), and analysis of the dislocations and their number N_D from a Voronoi tesselation (right).

the parabolic law of shrinkage (Eq. (3)) should hold during coupled GB migration, but with a reduced mobility M^* different from $M_n\Gamma$ [5,7].

2.3 Grain boundary sliding

Grain rotation without the requirement for continuity of crystal rows is called GB sliding [5,7], see Figure 1c. In this case, the tangential velocity is given by

$$v_t = -M_t \frac{\Gamma'}{R}, \tag{9}$$

where $\Gamma' = \mathrm{d}\Gamma/\mathrm{d}\theta$ and M_t is the mobility associated with tangential motion [5,7]. As for a circular grain $v_t = R\mathrm{d}\theta/\mathrm{d}t$, one has

$$\frac{\mathrm{d}\theta}{\mathrm{d}t} = -M_t \frac{\Gamma'}{R^2}. \tag{10}$$

Since one expects $\Gamma' > 0$ at low θ at least, the rotation occurs towards lower angles [5], which clearly differs from coupled GB migration (see Fig. 1c).

3 Experimental details

The experiment has been introduced in reference [20], so only the essentials will be recapped here.

3.1 Colloidal system

The colloidal dispersion consists of 2.82 μm diameter melamine-formaldehyde spheres (Microparticles), dispersed in an aqueous solvent, and contained in a 200 μm thick quartz cell (Hellma Analytics). As their gravitational height is very small (about 3% of the particle diameter), the particles sediment to the bottom wall of the cell within a few minutes to form a monolayer with negligible out-of-plane fluctuations. Within these conditions, it has been previously shown that this system behaves as two-dimensional hard spheres [22,23]. When the area fraction exceeds 0.73, a polycrystalline monolayer is obtained and the samples are left to coarsen until the crystalline grains are larger than the field of view, which effectively appears as covered by a single crystal (see Fig. 2a, left).

3.2 Creation of grain boundary loops using optical vortices

In order to create artificial GB loops in our two-dimensional colloidal crystal, we use the holographic

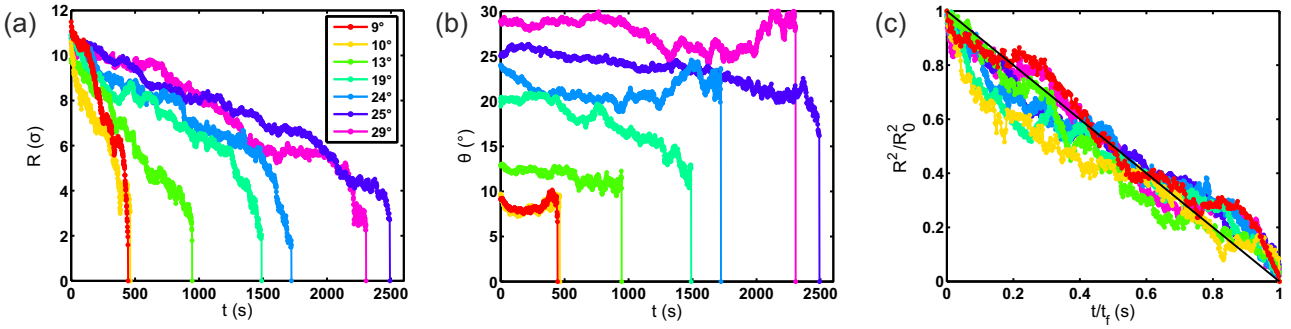

Fig. 3. (a) Time-evolution of the radius of GB loops with different initial misorientations and similar initial radii $R_0 = 10.8 \pm 0.5\sigma$. (b) Time-evolution of the misorientation for the same data as in (a). (c) Direct test of the scaling of parabolic shrinkage (black solid line, see text), where t_f is the time for complete shrinkage of each GB loop.

tweezing method described in reference [20]. An optical vortex [24,25] is generated using a spatial light modulator and is applied to the pristine crystal. The combined trapping force and angular momentum of the vortex induce the rotation of a circular portion of the crystal as shown in Figure 2a (centre), at a typical speed of 0.3 °/s. When the desired misorientation is reached, the beam is blocked to stop the rotation. The obtained grain is then free from external forces and starts shrinking (see Fig. 2a, right).

3.3 Identification of the grain boundary loop

From microscopy images similar to Figure 2a (right), the positions of the particles are detected using standard Matlab routines [26]. We then quantify the local crystalline order of a particle j by using the bond-orientational order parameter [27], $\psi_6^j = \left\langle e^{\mathrm{i}6\Delta\theta_{jk}} \right\rangle_k$, where the average runs over the nearest neighbours of j defined by a Delaunay triangulation and $\Delta\theta_{jk}$ are the corresponding bond angles. Subsequent coarse-graining of the ψ_6-field over two shells of nearest neighbours was found to improve the quality of the results [28]. The local crystal orientation is then given by $\theta_6 = \arg(\psi_6)/6$ and is shown in Figure 2b (left).

From the values of θ_6 we can discriminate the particles belonging to the central circular grain and the outer crystal. It is then possible to detect the particles belonging the GB loop, respectively at its inner and outer edges (see Fig. 2b, centre) [29]. Finally, the 5- and 7-coordinated particles are detected. The dislocations, which are pairs of 5- and 7-coordinated defects along the GB loop, can then be directly visualised using a Voronoi tessellation, as shown in Figure 2b (right).

This information enables us to extract the relevant quantities to study the GB loop kinetics, illustrated in Figure 2b:

- the radius of the GB loop in units of σ, $R = \sqrt{N_G/\pi}$, where N_G is the number of particles belonging to the grain and the inner GB edge;
- the misorientation of the GB loop, $\theta = \min(|\theta_6^{\mathrm{in}} - \theta_6^{\mathrm{out}}|, 60° - |\theta_6^{\mathrm{in}} - \theta_6^{\mathrm{out}}|)$, where θ_6^{in} and θ_6^{out} are respectively the average orientations of the particles in the central grain and the outer crystal, excluding the GB particles;
- the number of dislocations along the GB loop, N_D, and their density $\rho_D = N_D/(2\pi R)$ in units of σ^{-1}.

4 Results and discussion

4.1 Formation of grain boundary loops

In reference [20], we showed that the deformation induced by the optical vortex is not always followed by the formation of a GB loop. Indeed, the latter depends on the values of the GB loop radius and misorientation when the vortex is switched off, R_0 and θ_0. In particular, GB loops can be obtained only if

$$R_0\theta_0 \geq \frac{3}{\pi}\sigma, \tag{11}$$

where σ is the lattice spacing. In these conditions, the crystal is plastically deformed by the vortex, and a GB loop remains after it is turned off. Conversely, if $R_0\theta_0 < 3\sigma/\pi$, the initial crystal is elastically restored and no GB loop is formed.

As shown in reference [20], this fundamental limit is imposed by the specific dislocation structure of GB loops. In short, the six symmetric directions of the lattice and the circular shape of the GB impose that the minimal number of dislocations contained in a circular GB loop is six. For the GB loop to exist, the dislocation spacing imposed by the misorientation, $D = \sigma/\theta$ [30], cannot exceed the available spacing, equal to one sixth of the loop perimeter. Setting $D \leq \pi R/3$ thus leads to $R\theta \geq 3\sigma/\pi$, which is equation (11). In the remainder of this article, the initial conditions are set to satisfy equation (11) so that a GB loop is always formed after the vortex is turned off.

4.2 Reduced mobility

A GB loop that satisfies equation (11) spontaneously shrinks after the vortex is turned off ($t = 0$). We quantify the kinetics of shrinkage by monitoring the time-evolution of the radius R of GB loops with fixed initial radius $R_0 = 10.8 \pm 0.5\sigma$, and varying initial misorientations θ_0

in the range $[9°, 30°]$. As shown in Figure 3a, R decreases monotonically before it sharply drops to zero. Clearly, shrinkage takes longer upon increasing the initial misorientation. The time-evolution of the misorientation θ in Figure 3b shows that the misorientation is not always constant, but displays periods of increase and decrease during the shrinkage. This indicates the presence of grain rotation and thus the occurrence of multiple mechanisms of shrinkage, which we will discuss later.

Despite this complexity in the shrinkage process, the parabolic law of shrinkage given in equation (3) still applies [20]. Indeed, the data in Figure 3c show a good agreement with the master curve, $R^2/R_0^2 = 1 - t/t_f$, where $t_f = R_0^2/(2M^*)$ is the time corresponding to the end of shrinkage. In particular, the loop area decreases at constant rate $2\pi M^*$ according to equation (4) for all misorientations. The validity of the parabolic law means that shrinkage can be characterised by a *single* kinetic coefficient, the reduced mobility M^*. However, it does not necessarily imply that shrinkage is purely curvature-driven as other mechanisms can also lead to this behaviour [5,7]. In fact, the variations of θ in Figure 3b and the fluctuations around the master curve in Figure 3c, suggest the presence of various mechanisms, which we describe hereafter.

4.3 Kinetics of small angle grain boundary loops

In order to identify the mechanisms of grain shrinkage at stake, we first focus on the case of a GB loop with a relatively small initial misorientation, a "small angle" GB loop (SAGB loop). For this analysis, we carefully checked that we only used GB loops with an ideal dislocation structure, i.e. a null net Burgers vector [20], throughout the experiment. As a representative example, we show the time-evolution of the radius R, the number of dislocations N_D, and the misorientation θ, for a SAGB loop with $R_0 = 8.9\sigma$ and $\theta_0 = 9.6°$ in Figure 4a. While the grain keeps shrinking (R goes down), the evolution of θ exhibits three distinct phases: a decrease at early time ($t < 40s$, phase I), an increase at intermediate times ($40s < t < 300s$, phase II) and another decrease at late times ($t > 130s$, phase III). Strikingly, the behaviour of N_D is also characterised by three phases over the same time periods: it decreases in phase I, remains constant in phase II, and decreases again in phase III.

4.3.1 Phase I

In this phase, the grain shrinks while rotating to *lower* misorientations, which is reminiscent of curvature-driven shrinkage combined with GB sliding. Since Γ is usually an increasing function of θ, GB sliding is a way to decrease the interfacial free energetic cost [7].

4.3.2 Phase II

Figure 4a shows that in this phase the conservation of the number of dislocations corresponds to grain rotation towards *larger* misorientations. This seems counter-intuitive since it may lead to an increase of Γ [7]. To explain this behaviour, we recall that the number of dislocations is given by $N_D = 2\pi R/D$, where D is the dislocation spacing. Using the expression $D = \sigma/\theta$ [30], one obtains

$$N_D = \frac{2\pi R\theta}{\sigma}. \tag{12}$$

When N_D is conserved, it follows from equation (12) that

$$R(t)\theta(t) = C, \tag{13}$$

where C is a constant. As a consequence, when R decreases in time, θ has to increase because of the conservation of the number of dislocations, consistently with our observations.

It appears that equation (13) is nothing but equation (8) in the limit of small misorientations for which $\sin(\theta/2) \simeq \theta/2$. This confirms that phase II can be clearly identified as *coupled* GB migration. Indeed, the quantity $R\sin(\theta/2)$ is constant during this period, as one can see from Figure 4b. Since the number of dislocations is conserved during coupled GB migration, shrinkage is achieved without dislocation reactions, which corresponds to the preserved continuity of crystal rows. This therefore leads to an increase of the dislocation density ρ_D, as evident from Figure 4b. Indeed, inspection of the two snapshots in Figure 4c shows that the GB loop is made of six dislocations that are getting closer to each other as θ becomes larger.

We emphasize that equation (11) is not only expected to hold at the onset of GB loop formation, but also throughout shrinkage, as long as the GB loop is circular. We thus expect $R\sin(\theta/2) \simeq R\theta/2$ to be greater than $3\sigma/(2\pi) \simeq 0.48\sigma$ at all times. This is indeed true in phases I and II (see Fig. 4b), and we note than this lower bound is even reached during phase II. This is because the GB loop contains 6 dislocations (see Figs. 4a and 4c), which is the minimum for a circular GB [20].

4.3.3 Phase III

In this phase $R\sin(\theta/2)$ goes below the lower bound of 0.48σ and decays to zero. One can also see from Figure 4a that N_D goes below 6. To explain this apparent paradox, we recall that equation (11) only holds for dislocations resulting from a purely rotational deformation of a hexagonal crystal. This deformation imposes a circular shape that in turns leads to six or more dislocations, owing to the hexagonal symmetry of the crystal. As a consequence, the fact that equation (11) is not respected in phase III means that the present set of dislocations cannot be obtained directly from a rotational deformation of the crystal. Instead, it results from the kinetic pathway taken during shrinkage. These remaining dislocations are annihilated via a series of dislocation recombinations [5,20], shown in Figure 4d, until the perfect crystal is recovered. Note that despite the apparent decrease of θ, phase III should not be confused with GB sliding since the GB loop character is in fact lost.

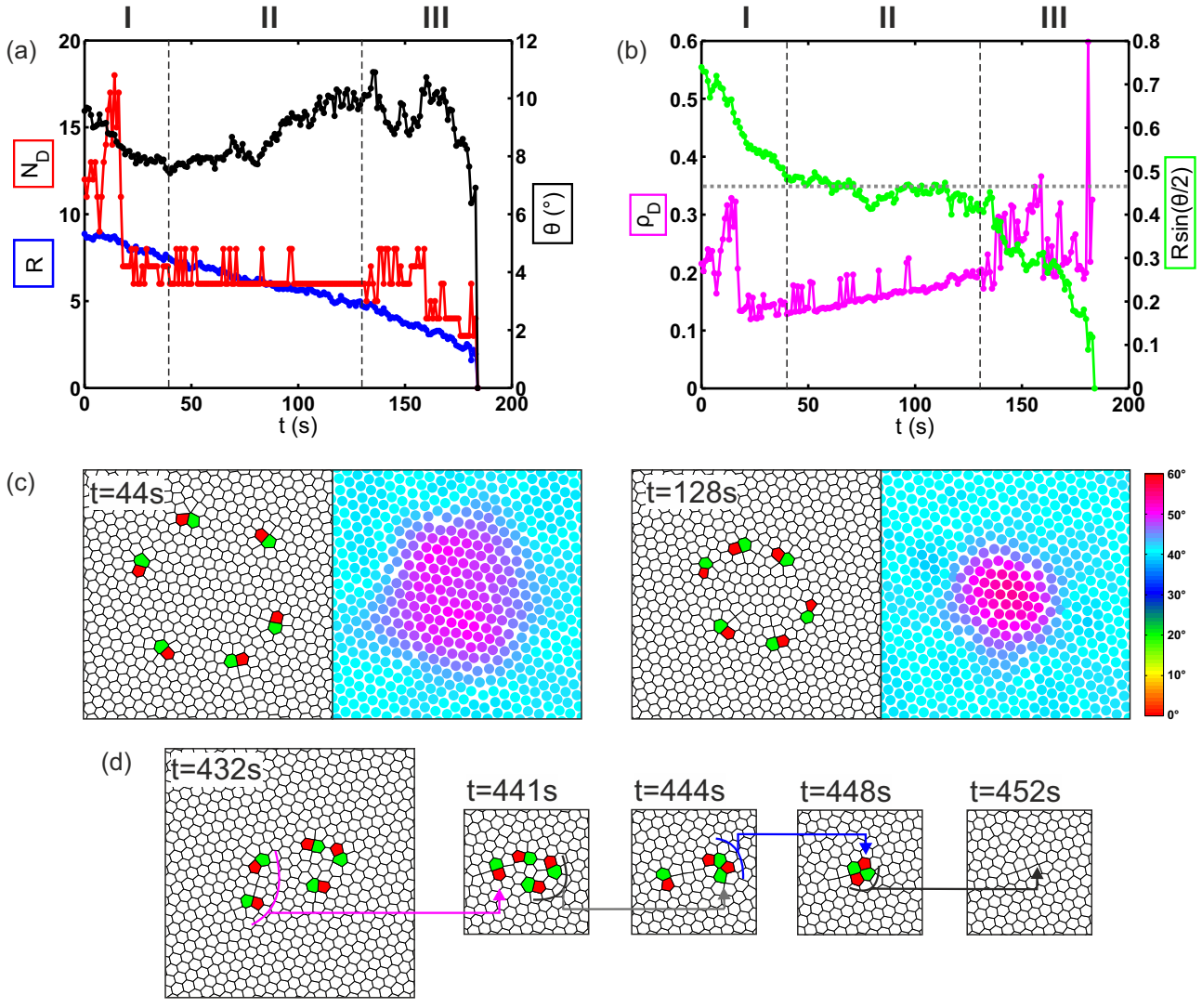

Fig. 4. (a) Time-evolution of the radius of the grain (R), the number of dislocations along the GB (N_D), and the misorientation (θ) for a SAGB loop. The behaviour can be decomposed into the phases I, II, and III. The initial radius and misorientation are $R_0 = 8.9\sigma$ and $\theta_0 = 9.6°$. (b) Time-evolution of the dislocation density ρ_D and $R\sin(\theta/2)$. The horizontal grey dotted line corresponds to the lower bound given by equation (11). (c) Voronoi tesselations showing the dislocations at the GB loop together with the orientation maps at the beginning and at the end of coupled migration (phase II). (d) Final stages of shrinkage when the GB loop character is lost (phase III). The assembly of dislocations is annihilated via dislocation reactions (arrows). The data correspond to a SAGB loop with $R_0 = 10.8\sigma$ and $\theta_0 = 9°$ (red curve in Fig. 3) for which phases I, II, and III also apply, with phase III starting around $t \simeq 400$ s.

4.4 Kinetics of large angle grain boundaries

We now look at the case of a "large angle" GB loop (LAGB loop), reported in Figure 5a, where $R_0 = 10.8\sigma$ and $\theta_0 = 19.5°$. One can see that R decreases monotonically in this case as well, but shrinkage takes much longer than for the SAGB loop, mostly due to the higher misorientation (rather than the initial size difference, which remains relatively small). The grain orientation θ is constant up to $t = 500$ s (phase I), and then decreases until shrinkage is complete (phase II[1]). Overall, N_D decreases and so is $R\sin(\theta/2)$, as one can see from Figure 5b.

These observations point towards the following mechanism for shrinkage: in phase I, pure curvature-driven shrinkage dominates since θ is constant. In phase II, shrinkage is accompanied by GB sliding, which reduces Γ. This can be seen from the snapshots in Figure 5c, where both the grain size and misorientation have decreased over time. Note that in phase II, two plateaus are visible for $R\sin(\theta/2)$, which correspond to the presence of phases of coupled GB migration. They last for about 100 s each, which is consistent with the duration of coupled GB migration in the case of the SAGB loop.

[1] Note that the phases I and II for the LAGB loop do not imply that the same mechanisms as in phases I and II for the SAGB loop occur. These numbers are only used as labels for specific time periods in each case.

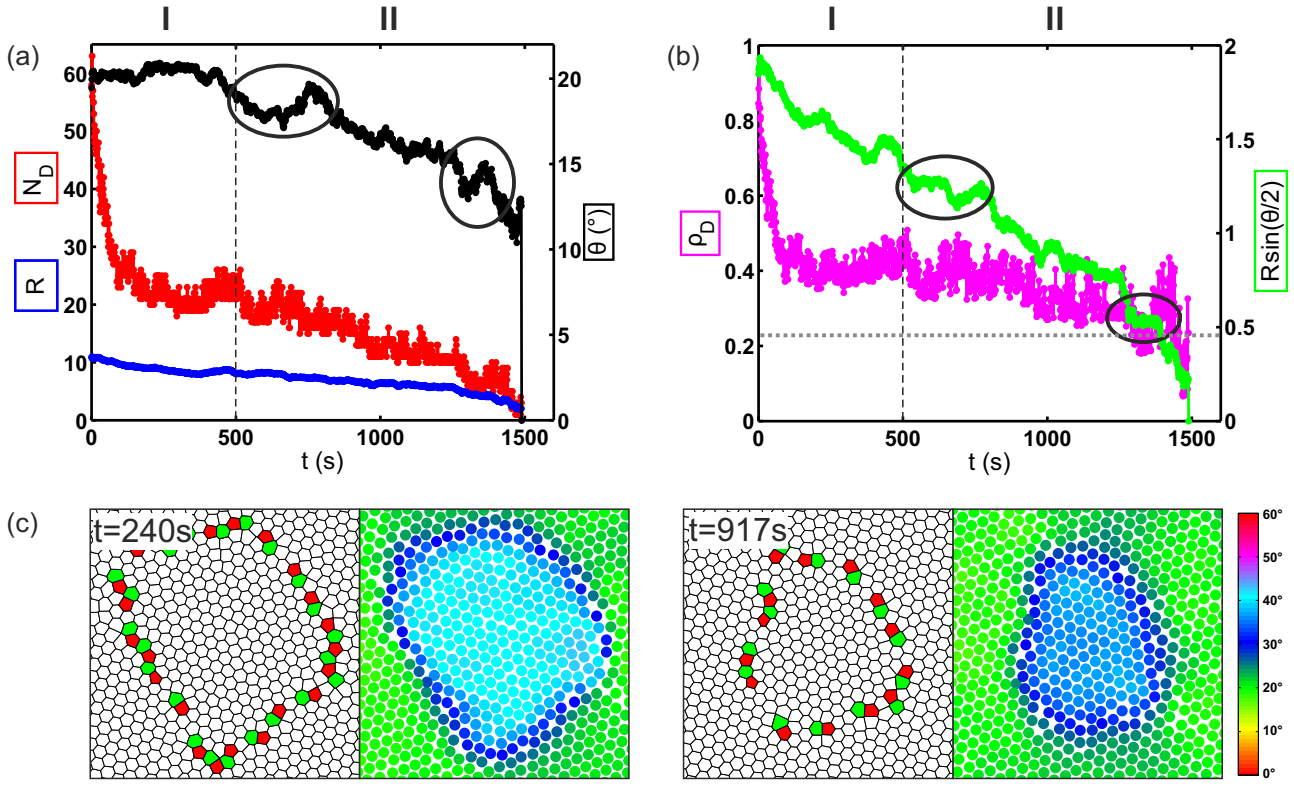

Fig. 5. (a) Time-evolution of the radius of the grain (R), the number of dislocations along the GB (N_D), and the misorientation (θ) for a LAGB loop. The behaviour can be decomposed into two phases I and II. Periods of coupled GB migration are circled in black. The initial radius and misorientation are $R_0 = 10.9\sigma$ and $\theta_0 = 19.5°$. (b) Time-evolution of the dislocation density ρ_D and $R\sin(\theta/2)$. The horizontal grey dotted line corresponds to the lower bound given by equation (11). (c) Voronoi tesselations showing the dislocations at the GB loop together with orientation maps at two different times during shrinkage.

Comparing Figures 5b with 4b show that the density of dislocations ρ_D is much higher for the LAGB than for the SAGB loop. This is also obvious by directly comparing the distribution of dislocations in Figure 5c for the LAGB loop and Figure 4c for the SAGB loop. Importantly, ρ_D is roughly constant during most of the shrinkage of the LAGB loop. This indicates that the main mechanism to reduce the loop size is the annihilation of dislocations, consistent with the overall drop of N_D and the loss of continuity in the crystal rows. However, these dislocation reactions would be difficult to observe due to the high density of dislocations.

Consistently with the lower bound on $R\theta$ given by equation (11), $R\sin(\theta/2)$ is above 0.48σ throughout shrinkage as well. Only close to the end of shrinkage does this quantity go below the threshold, after the last phase of coupled GB migration. This corresponds to the point where the GB loop character is lost as N_D drops below 6, analogous to phase III of the SAGB loop.

5 Conclusion

In summary, we have shown that three modes of GB migration proposed in reference [7] for atomic materials hold in colloidal materials as well. In particular, we have experimentally demonstrated the presence of purely curvature-driven migration, coupled GB migration, and GB sliding during the shrinkage of GB loops in a two-dimensional colloidal crystal with simple hard sphere interactions. These three mechanisms contribute intermittently to the shrinkage process. The product $R\theta$ is always above its predicted lower bound of $3\sigma/\pi$ in the case of GB loops throughout shrinkage. Only towards the end this is no longer the case, when the GB loop character is lost.

The variety of mechanisms at play suggest a description of the GB loop kinetics in terms of the many associated coefficients, such as M_n, M_t, and Γ, which are all functions of the GB loop parameters, R and θ. However, despite this complexity, we have shown that the description can be simplified by using a single kinetic coefficient, the reduced mobility M^*. In reference [20], we have experimentally demonstrated that M^* is a function of the sole product $R_0\theta_0$, namely $M^* = (A(R_0\theta_0 - 3\sigma/\pi))^{-1}$ where A is a constant. The first important consequence is that the description of GB loop kinetics may be reduced to finding the material-specific constant A. The second consequence is that the rate of shrinkage (essentially M^*) is solely determined by the number of dislocations at the time of GB loop formation, since $R_0\theta_0$ is proportional to N_D according to equation (12), at least for low θ. The fact that M^* is a sole function of $R_0\theta_0$ has been shown in the case of coupled GB migration using simulations [12],

however, our results suggest that this may be a more general feature of GB loop kinetics.

The European Research Council (ERC) is acknowledged for financial support (ERC Starting Grant 279541-IMCOLMAT).

Author contribution statement

F.A.L. and R.P.A.D. designed the research. F.A.L. and A.C. performed the experiments. F.A.L. analyzed the data. A.C. developed the optical tweezing stage and protocols. All authors interpreted the results. F.A.L. and R.P.A.D. wrote the manuscript. All the authors have read and approved the final manuscript.

References

1. G. Gottstein, L.S. Shvindlerman, *Grain boundary migration in metals: thermodynamics, kinetics, applications* (CRC Press, Boca Raton, USA, 1999)
2. R.C. Sun, C.L. Bauer, Acta Metall. Mater. **18**, 638 (1970)
3. R. Viswanathan, C.L. Bauer, Acta Metall. Mater. **21**, 1109 (1973)
4. K. Honda, Jpn. J. Appl. Phys. **26**, 637 (1987)
5. Z.T. Trautt, Y. Mishin, Acta Metall. Mater. **60**, 2424 (2012)
6. L.A. Barrales-Mora, J.-E. Brandenburg, D.A. Molodov, Acta Metall. Mater. **80**, 148 (2014)
7. J.W. Cahn, J.E. Taylor, Acta Metall. Mater. **52**, 4898 (2004)
8. E. Cockayne, Phys. Rev. B **85**, 125409 (2012)
9. W.W. Mullins, J. Appl. Phys. **27**, 904 (1956)
10. C.L. Di Prinzio, B.J. Gonzalez Kriegel, O.B. Nasello, Acta Metall. Mater. **43**, 2273 (1995)
11. A.E. Lobkovsky, A. Karma, M.I. Mendelev, M. Haataja, D.J. Srolovitz, Acta Metall. Mater. **52**, 292 (2004)
12. A. Adland, Y. Xu, A. Karma, Phys. Rev. Lett. **110**, 265504 (2013)
13. K.-A. Wu, P.W. Voorhees, Acta Metall. Mater. **60**, 419 (2012)
14. S. Kurasch, J. Kotakoski, O. Lehtinen, V. Skákalová, J. Smet, C.E. Krill, A.V. Krasheninnikov, U. Kaiser, Nano Lett. **12**, 3173 (2012)
15. C. Gong, K. He, Q. Chen, A.W. Robertson, J.H. Warner, ACS Nano **10**, 9173 (2016)
16. H.M. Lindsay, P.M. Chaikin, J. Chem. Phys. **76**, 3781 (1982)
17. R.P.A. Dullens, C. Bechinger, Phys. Rev. Lett. **107**, 138301 (2011)
18. W.T.M. Irvine, A.D. Hollingsworth, D.G. Grier, P.M. Chaikin, Proc. Natl. Acad. Sci. U.S.A. **110**, 15548 (2013)
19. C.E. Cash, J. Wang, M.M. Martirossyan, B.K. Ludlow, A.E. Baptista, N.M. Brown, E.J. Weissler, J. Abacousnac, S.J. Gerbode, Phys. Rev. Lett. **120**, 018002 (2018)
20. F.A. Lavergne, A. Curran, D.G.A.L. Aarts, R.P.A. Dullens, Proc. Natl. Acad. Sci. U.S.A. **115**, 6927 (2018)
21. C. Herring, in *The Physics of Powder Metallurgy*, edited by W.E. Kingston (McGraw-Hill, New York, 1951), p. 143
22. A.L. Thorneywork, R. Roth, D.G.A.L. Aarts, R.P.A. Dullens, J. Chem. Phys. **140**, 161106 (2014)
23. A.L. Thorneywork, J.L. Abbott, D.G.A.L. Aarts, R.P.A. Dullens, Phys. Rev. Lett. **118**, 158001 (2017)
24. D.G. Grier, Nature **424**, 816 (2003)
25. J.E. Curtis, D.G. Grier, Phys. Rev. Lett. **90**, 133901 (2003)
26. D. Blair, E. Dufresne, *The matlab particle tracking code repository*, retrieved from http://physics.georgetown.edu/matlab/
27. D.R. Nelson, *Defects and geometry in condensed matter physics* (Cambridge University Press, Cambridge, UK, 2002)
28. F.A. Lavergne, D.G.A.L. Aarts, R.P.A. Dullens, Phys. Rev. X **7**, 041064 (2017)
29. F.A. Lavergne, D.G.A.L. Aarts, R.P.A. Dullens, J. Phys.: Condens. Matter **27**, 194117 (2015)
30. J.M. Howe, *Interfaces in materials: atomic structure, thermodynamics and kinetics of solid-vapor, solid-liquid and solid-solid interfaces* (Wiley-Interscience, New York, USA, 1997)